crystals

MDPI

Article

Si Quantum Dots Assist Synthesized Microflower-Like Si/MoS_2 Composites for Supercapacitors

Jiahong Zheng [1,2,*], Kangkang Cheng [1,*], Runmei Zhang [1], Yamei Yang [1], Yuntao Wu [1] and Pengfei Yu [1]

1 School of Materials Science and Engineering, Chang'an University, Xi'an 710064, China; zrm199307012222@163.com (R.Z.); 2019131034@chd.edu.cn (Y.Y.); kilo980112@gmail.com (Y.W.); yupengfei@chd.edu.cn (P.Y.)

2 Engineering Research Central of Pavement Materials, Ministry of Education, Chang'an University, Xi'an 710064, China

* Correspondence: jhzheng@chd.edu.cn (J.Z.); 2018231026@chd.edu.cn (K.C.); Tel.: +86-029-8233-7340 (J.Z.)

Received: 15 August 2020; Accepted: 20 September 2020; Published: 22 September 2020

Abstract: The microflower-like Si/MoS_2 composites were fabricated using Si quantum dots (QDs) to assist a facile hydrothermal method. The electrochemical performance of Si/MoS_2 composite in symmetric and asymmetric systems was studied. Electrochemical characterization revealed that the Si/MoS_2 composite electrode in a three-electrode system has a high specific capacitance of 574.4 $F{\cdot}g^{-1}$ at 5 $A{\cdot}g^{-1}$. Furthermore, the Si/MoS_2 composite electrode in a two-electrode system had the maximum energy density of 27.2 $Wh{\cdot}kg^{-1}$ when a power density of 749.1 $W{\cdot}kg^{-1}$ was achieved. Therefore, this investigation proves the Si/MoS_2 composite microflower-like structure should be a promising candidate electrode material for supercapacitors.

Keywords: Si/MoS_2; electrochemical performance; supercapacitor

1. Introduction

The progress of science and technology has brought about rapid changes to human life, but has also brought about irreversible problems, such as global warming, the near exhaustion of non-renewable energy, and environmental pollution. Humans are eager to seek new, green energy to alleviate the energy crisis and environmental crisis, and even replace the traditional non-renewable energy [1–3]. Clean energy storage devices have been widely researched, due to their wider and wider application in numerous electronic devices. As a new type of clean energy storage device, supercapacitors have high power density, good cyclic stability, fast charge, and high rate of discharge [4–8].

Nowadays, two-dimensional (2D) materials have shown many unique advantages. Firstly, because electrons are confined to the 2D plane, especially for monolayer 2D materials, their electronic properties are enhanced. Therefore, 2D materials are ideal materials for basic research in condensed matter physics and electronic/optoelectronic devices. Secondly, because 2D materials can maintain the thickness of atoms while possessing the maximum plane size, they have a large specific surface area. This property has greatly attracted research into applications concerning surface area, such as catalysis and supercapacitors. Thirdly, ultra-thin 2D nanomaterials based on liquid phase processing can be prepared by simple methods into a single high-quality film, which is very necessary for practical applications, such as supercapacitors and solar cells.

2D transition metal disulfides (TMDs) have attracted widespread attention, due to their special layer structure. They have better performance of conductivity and larger surface area than oxide, the metal element and sulfur element through the weak van der Waals force of interaction between a

single layer, forming a similar graphene layer structure [9]. This structure facilitates the insertion and extraction of various ions, and can be developed in the field of energy storage, including for lithium ion batteries and supercapacitors. Transition metal sulfides (MoS_2 [10] CoS [11], NiS [12], CuS [13], etc.) are considered as potential materials for electrodes, because of their wide range of sources, low prices, and unique physicochemical properties. As a representative transition metal sulfide, MoS_2 has received extensive attention in capacitor research [14]. Manuraj et al. [15] reported a specific capacitance of 972 $F{\cdot}g^{-1}$ at 1 $A{\cdot}g^{-1}$ for MoS_2-RuO_2 nanocomposite. Lien et al. [16] fabricated high voltage symmetric supercapacitors of graphene/MoS_2, which works at a wide operating voltage of 2.3 V and achieves the maximum energy density of 31.2 Wh kg^{-1}. Vattikuti et al. [17] reported that the hydrothermal reaction synthesized MoS_2/MoO_3 heterostructure electrodes have a high specific capacitance of 287.7 $F{\cdot}g^{-1}$ at 1 $A{\cdot}g^{-1}$ with good cycling stability. The MoS_2 preparation method is simple and low cost. MoS_2 has different morphologies, such as nanoball [18], nanoflake [19], nanoflower [20], nanofilament [21], nanoparticle [22], etc. It is found that MoS_2 can not only show good capacitance in the electrochemical double layer, but can also generate an extra Faraday capacitance, due to the interaction between Li^+, Na^+, K^+, and other ions inserted into the MoS_2 layer. Nevertheless, the energy storage application of pure MoS_2 as an electrode material is still very limited, with low conductivity and easy agglomeration, leading to a relatively low capacitance of MoS_2. Therefore, the current research focus is to improve the electrochemical performance and increase the capacitance of composite materials

Zero-dimensional semiconductor nanomaterials can be sorted into three categories: IV group quantum dots, III-V group quantum dots [23], and II-VI group quantum dots. In the IV group, Si is one of the most important elements. Si, one of the most important elements, is the eighth most abundant element in the universe. Si nanomaterials are fully compatible with Si-based microelectronic devices, and nanosilicates have many unusual optical and electrical properties [24]. As a result of high research value, both in the basic theory and practical applications, Si nanomaterials have attracted considerable attention. The quantum confinement effect occurs when the particle size of a Si nanocrystal is reduced to the radius of the exciton Bohr. Si nanocrystals are then called Si QDs. In Si QDs, the motion of electrons or holes in three-dimensional space is constrained by the fact that the constrained carrier can only be located at the separated bound level, and the motion is fully quantized, thus weakening the constraint of momentum conservation. Therefore, the electronic structure of Si semiconductor nanocrystals is different from that of bulk materials of the same composition. It is mainly manifested in the enhancement of electron–hole exchange, the increase of exciton binding energy, and the increase of optical transition oscillation intensity with the decrease of semiconductor gap width. Among the quantum constraint effects, the most reported is the quantum size effect, that is, the band gap increases as the quantum dot size decreases. Si QDs have been developed in recent years with many advantages. The low preparation cost lays a foundation for the rapid application of Si QDs in production. Its low toxicity provides a security guarantee for the experimental research of Si QDs [25]. Its chemical properties provide a basis for the study of its electrochemical properties.

In this article, we propose a scheme for the synthesis of MoS_2 using Si QDs to assist hydrothermal synthesis. Using the Si QDs as the center of nucleation promotes the nucleation process of MoS_2, and accelerates the reaction speed. Si/MoS_2 composite presents a flower-like structure, with the petals crisscrossing each other. This structure makes the active substance fully contact the electrolyte, which results in the redox reaction. Moreover, to a certain extent, the structure reduces the changes in the microstructure of the material caused by the charging and discharging process. By comparing the electrochemical performance of the two kinds of electrodes (MoS_2 and Si/MoS_2 composite), the Si/MoS_2 composite electrode demonstrates excellent performance, including high specific capacitance and good cyclic stability. This work can arouse wide interest in the preparation of high-performance mixed-metal sulfide electrode materials by a simple method.

2. Materials and Methods

A total of 0.1 g of sodium ascorbate was dissolved in 10 mL deionized (DI) water while stirring for 30 min, then, a solution could be obtained. Following this, 3.75 mL of sodium ascorbate solution, 1 mL of N-aminoethyl-γ-aminopropyltrimethoxysilane, and 12 mL DI water were mixed with magnetic stirring for 20 min to obtain a Si quantum dot solution.

Firstly, 0.7062 g $(NH_4)_6Mo_7O_{24}{\cdot}6H_2O$ and 1.3049 g H_2NCSNH_2 were diluted with 20 mL DI water. The prepared solution was mixed with 1 mL Si QD solution, and subjected to continuous magnetic stirring for 1 h. Subsequently, the reaction mixture was kept in a Teflon lined stainless steel autoclave at 180 °C for 18 h. After that, the final mixture product was filtered, washed with DI water, and dried at 60 °C in a vacuum oven to obtain the Si/MoS_2 composite. For better comparison, the MoS_2 was prepared following the same procedures, but without the Si QDs.

An electrochemical station (CHI 660E, Chenhua, Shanghai, China) was taken to test electrochemical performance in 6 M KOH. The sample was used as the working electrode, with a platinum foil (2 cm × 2 cm) and a saturated calomel electrode as the counter and the reference electrode, respectively. The specific capacitance of the single electrode was calculated using the equation:

$$C = i\Delta t/(S\Delta V) \quad (1)$$

$$C = i\Delta t/(m\Delta V) \quad (2)$$

where C is the specific capacitance, i is the discharge current, Δt is the discharge time, S and m are assigned as the area and mass of the electrode material, and ΔV represents the potential window.

3. Results

Fourier transform infrared (FT-IR) spectroscopy (TENSOR II, Bruker, Karlsruhe, Germany) was used to investigate the bonding interaction and functional groups of samples [26]. As shown in Figure 1a, the peak appearing at 590 cm^{-1} is assigned to the Mo–S vibration [27], the peak at 1010 cm^{-1} corresponds to the S–O stretching [28], and the peak at 1413 cm^{-1} is attributed to C–O stretching vibration [29]. For MoS_2, the peaks observed at 1132 and 1651 cm^{-1} are attributed to the C–H bending vibration [27] and the existence of C=O stretching vibration [30]. For Si/MoS_2, the absorption peak at 1106 cm^{-1} is ascribed to the characteristic stretching of the Si–O–Si band [31]. Figure 1b gives the XRD pattern for Si/MoS2 composite. The main diffraction peaks of MoS2 at 2θ = 33.3°, 39.2° and 48.5° correspond to (101), (103), and (105) reflections, respectively (JCPDS card no. 37-1492). The peak of Si at 2θ = 58.6° can be attributed to the (101) plane (JCPDS card no. 47-1186).

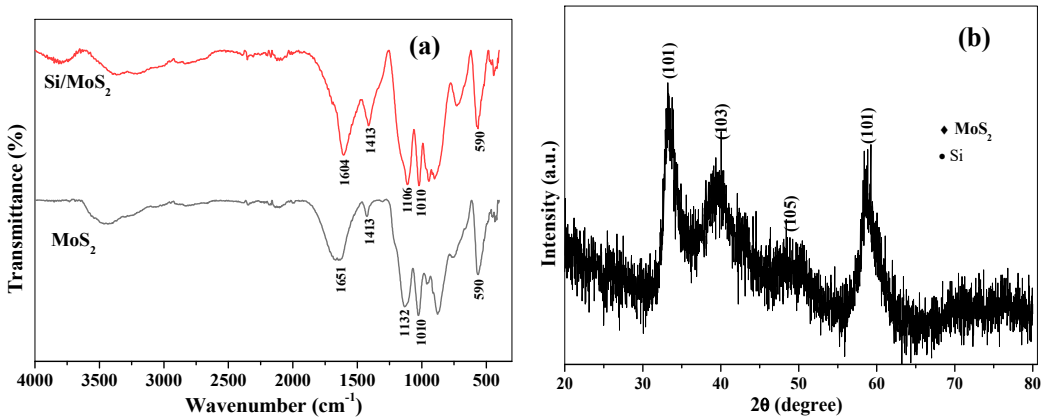

Figure 1. FT-IR spectrum of MoS_2 and Si/MoS_2 composite electrodes (**a**), and XRD pattern of Si/MoS_2 composite (**b**).

X-ray photoelectron spectroscopy (XPS, ESCA-LAB Mk II, VG Scientific Co., London, England) was used to analyze the elemental valence state and surface chemical composition. Figure 2 shows the XPS high-resolution spectra of Mo 3d and S 2p. The peaks at 230.3 eV, 233.5 eV, and 236.3 eV, observed in the pristine spectrum of Mo in Figure 2a, are identified as Mo^{4+} $3d_{5/2}$, Mo^{4+} $3d_{3/2}$, and Mo^{6+} $3d_{3/2}$, respectively [32]. The presence of Mo^{6+} indicates that there may be a small amount of MoO_3 in the sample [33]. Moreover, there is another peak at 227.1 eV, which represents S^{2-} 2s [34]. For S 2p in Figure 2b, the peaks at 163.7 eV and 164.2 eV, observed in the pristine spectrum of S, correspond to S $2p_{5/2}$ and S $2p_{3/2}$.

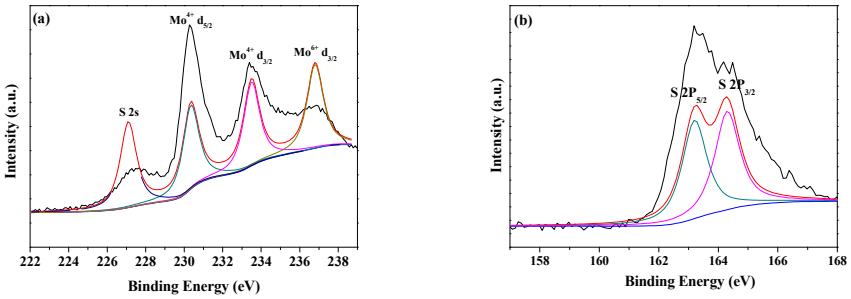

Figure 2. The XPS spectra of (**a**) the Mo 3d; and (**b**) the S 2p.

In order to study the effect of Si QDs on the microstructure of the whole composite, field emission scanning electron microscope (FESEM, S-4800, Hitachi, Tokyo, Japan) analysis was used for MoS_2 and Si/MoS_2 composite. Figure 3 shows the SEM images of MoS_2 and Si/MoS_2 composite. In Figure 3a–c, it can be seen that without Si QDs, MoS_2 is composed of irregular nanosheets with a diameter of 200–300 nm. Most of the nanosheets are tiled, and there are some curled-off phenomena. On the other hand, it still conforms to the rule that MoS_2 nanosheets tend to grow in flat under the control of MoS_2. Figure 3d,f is the SEM diagram of Si/MoS_2 composite material. After adding a small amount of Si QDs, the Si/MoS_2 composite presents a microflower spherical structure composed of staggered nanosheets, which indicates that the MoS_2 nanosheets grow with Si QDs as nucleation centers, and finally grow into three-dimensional flower spheres. The energy dispersive X-ray (EDX) elemental maps in Figure 3g–i reveal that there are Si, Mo, and S elements in the Si/MoS_2 composite. It is evident that the Si QDs are uniformly distributed in Si/MoS_2 composite.

A possible growth mechanism is depicted in the schematic diagram in Figure 4. Without Si QDs, MoS_2 tends to grow tiled in the direction with the minimum binding potential energy. With the prolongation of reaction time, the MoS_2 nanosheets grew more and more, and were stacked. A small part of MoS_2 nanosheets can overcome the crimping of partial binding potential energy or the semi-upright growth. It may be caused by the dynamic force generated by the easy agglomeration of MoS_2 itself, which can overcome the crimp growth of certain binding potential energy, and finally form the structure in Figure 3c; when, with Si QDs, due to the small size of Si QDs, it can be used as the nucleation center in the reaction process. The generated MoS_2 nanosheet tends to pile up around Si QDs, overcoming the potential energy for rapid three-dimensional growth, and finally forming a micron flower ball. As a result, the structure in Figure 3f is formed with the continuation of the reaction time.

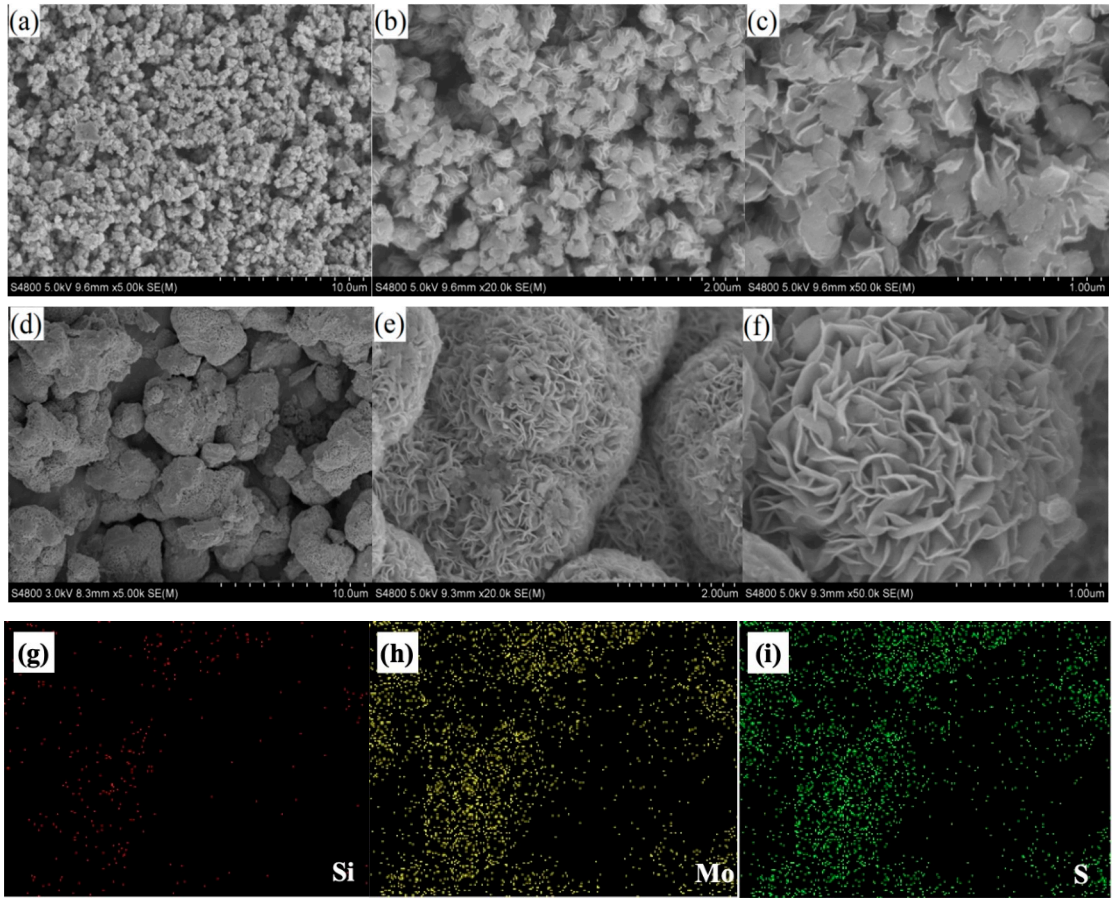

Figure 3. SEM images of MoS_2 (**a**–**c**), S and Si/MoS_2 composite (**d**–**f**), and EDX elemental mapping image of Si (**g**), Mo (**h**), and S (**i**) in Si/MoS2 composite.

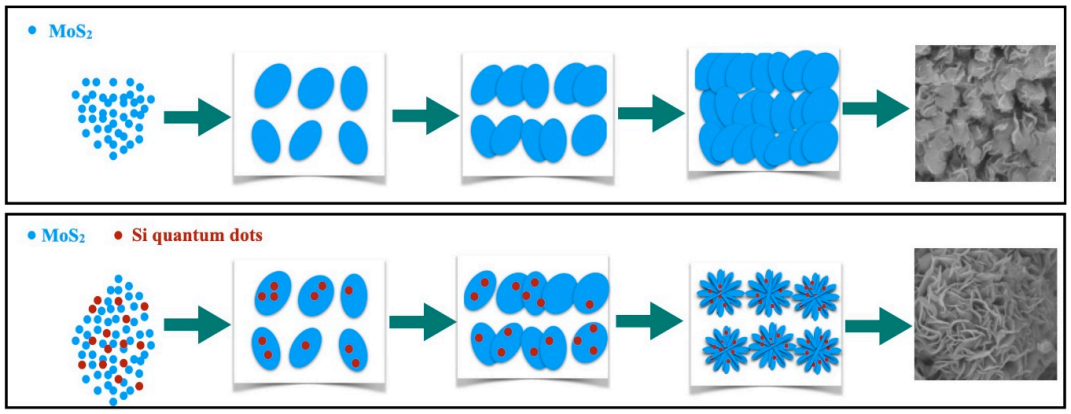

Figure 4. Schematic illustration of the formation for MoS_2 and Si/MoS_2 composite.

Figure 5a is the transmission electron microscope (TEM, Tecnai F30G2, FEI, Hillsboro, OR, USA) image of Si/MoS_2. It confirms the microflower structure further, in which many nanosheets are stacked on each other. The result is consistent with the SEM image in Figure 3f. Figure 5b is a high-resolution-TEM image of Si/MoS_2, in which it is clearly observable the ordered lattice fringes with the corresponding interplanar distance of 0.61 nm, which relates to the (002) plane of the MoS_2 [35]. Figure 5c is the high-resolution image after the Fourier transform of the box area in Figure 5b. The

crystal lattice of the sample can be observed to be 0.22 nm, which corresponds to the (100) plane of the MoS_2.

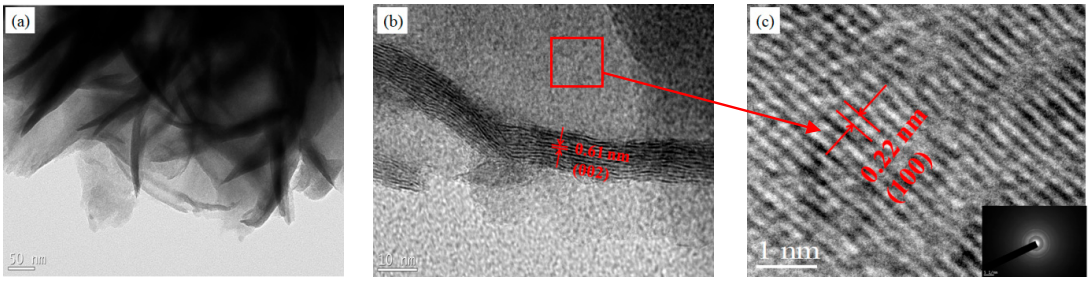

Figure 5. TEM image of Si/MoS_2 composite (**a**); high-resolution TEM images (**b**) and (**c**).

In order to compare the electrochemical properties of the MoS_2 and Si/MoS_2 composite, CV curves with a scan rate of 100 mV·s^{-1} were given in Figure 6a,b. In Figure 6a, the integral areas of the CV curve of the Si/MoS_2 composite are bigger than those of MoS_2, which suggests that the specific capacitance of Si/MoS_2 composite is bigger than the MoS_2. The GCD curves of the MoS_2 and Si/MoS_2 composite at the same current density of 50 A·g^{-1} are shown in Figure 6b. The plateaus in the GCD curves indicate that the two samples performed pseudocapacitor behaviors [36], which is consistent with the CV results. In Figure 6b, Si/MoS_2 composite possesses a longer discharge time than MoS_2, which indicates that it has a large specific capacitance. The specific capacitance of Si/MoS_2 composite is higher than that of MoS_2 for the following three reasons: (1) after the addition of Si QDs, Si QDs as the nucleation center, play the role of supporting MoS_2 nanosheets, which greatly increases the ion transport channel; (2) the porous and open microflower structure of Si/MoS_2 composite, which can shorten the diffusion path of electrons and ions and enhance electrochemical dynamics [37]; and (3) the open space of the Si/MoS_2 composite microflower can act as the robust reservoir for electrolyte ions, supplying sufficient redox reactions for energy storage [38]. The CV curves for MoS_2 and Si/MoS_2 composite at different scan rates of 5–100 mV/s are shown in Figure 6c,d. With the increase of the scanning rate, the peak of current gradually increased, and the curve shape remained basically unchanged in the CV curves of MoS_2 and Si/MoS_2 composite, indicating that the two electrode materials had the potential to provide high power performance. The GCD curves of the MoS_2 and Si/MoS_2 composite at different current densities are shown in Figure 6e,f. The specific capacitances of the MoS_2 and Si/MoS_2 composite can be calculated on the basis of the GCD curves, and the results are presented in Figure 6g. The specific capacitance of Si/MoS_2 composite at any of the same current densities is higher than that of MoS_2. With the increase of current density, the discharge time is shortened continuously, so the specific capacity is also decreased continuously. When the current density of Si/MoS_2 composite is at the 5 A·g^{-1}, 10 A·g^{-1}, 20 A·g^{-1}, 30 A·g^{-1}, 40 A·g^{-1}, and 50 A·g^{-1}, the corresponding specific capacitance of Si/MoS_2 composite electrode is 574.4 F·g^{-1}, 500.0 F·g^{-1}, 404.4 F·g^{-1}, 284.4 F·g^{-1}, and 233.3 F·g^{-1}, respectively, which is consistent with the analysis results of CV curves in Figure 6c,d. Figure 6i shows cyclic stability of capacitive performance of Si/MoS_2 electrode tested for 1000 cycles at 1 A·g^{-1}. The Si/MoS_2 composite electrode exhibits specific capacitance retention of 84.5% for 1000 cycles.

Nyquist plots of the MoS_2 and Si/MoS_2 composite electrodes are shown in Figure 6h. Generally, a semicircle in the high frequency region and a straight line with slope in the low frequency region are shown. In the low frequency region, it consists of a straight line, while in the high frequency region, it consists of a semicircle. The diameter of the semicircle is related to the charge transfer resistance (Rct). The radius of the Rct from the high frequency arc is on the real axis. Additionally, the smaller the radius, the smaller the Rct. A smaller Rct for Si/MoS_2 and a vertical line along the virtual axis show lower resistance and better capacitive behavior [39]. The Nyquist curve of the X-ray intercepts the equivalent series resistance of said electrode (R_S), which is 0.506 Ω.

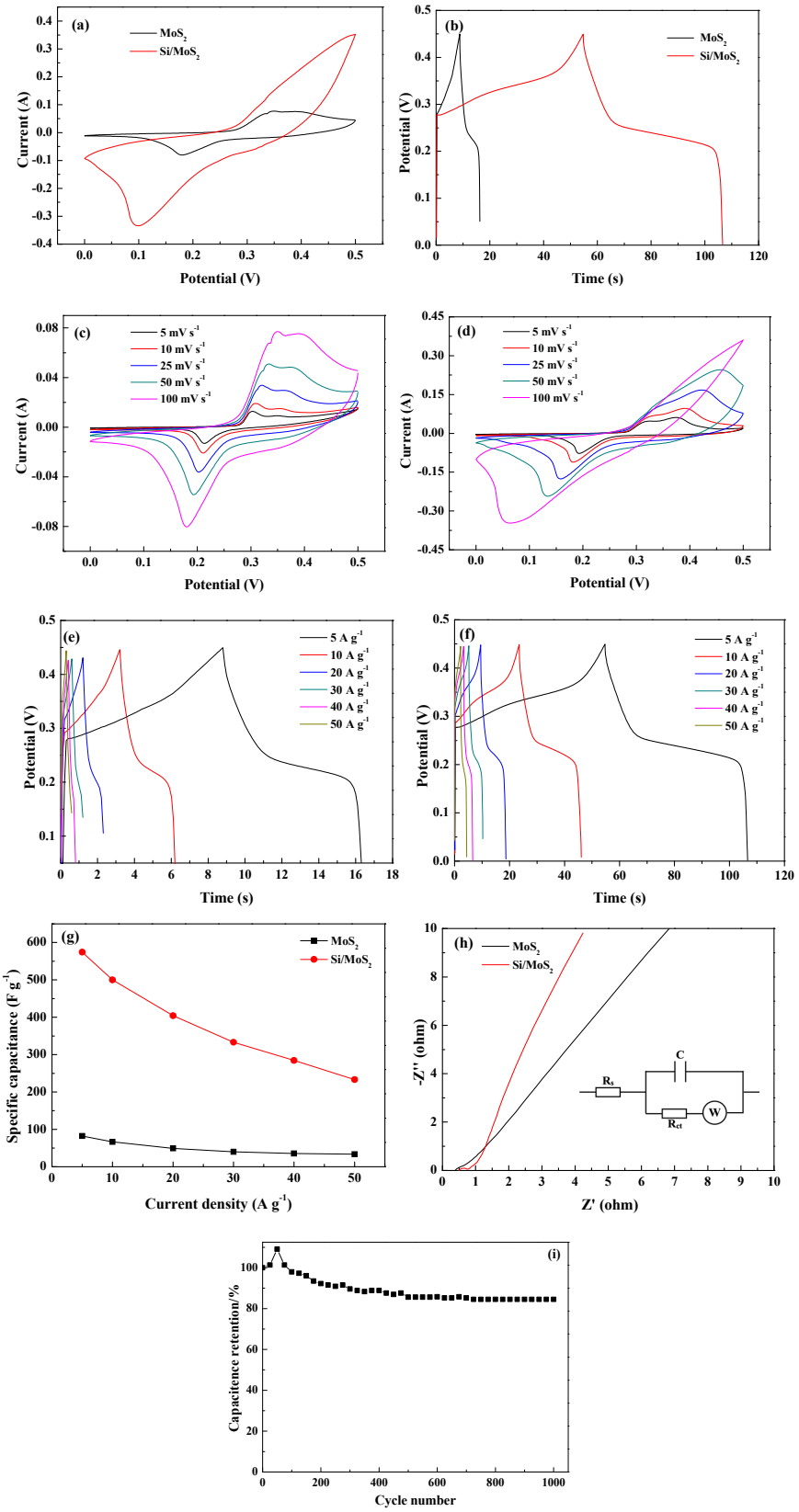

Figure 6. (**a**,**b**) Comparison of CV and GCD curves of two electrodes; (**c**,**e**) CV and GCD curves of MoS_2 and (**d**,**f**) Si/MoS_2 composite; (**g**) rate capacitance calculated by GCD curves; (**h**) EIS curves of two electrodes (the inset shows the equivalent circuit model used for fitting the EIS plot); (**i**) cyclic stability test at 1 A·g^{-1} for Si/MoS_2 composite electrode.

In order to evaluate the potential practical application of the Si/MoS_2 composite electrode, an asymmetric capacitor (Si/MoS_2//AC) was constructed, with Si/MoS_2 composite active material as positive electrode and AC as negative electrode, to investigate its electrochemical performance. An electrochemical workstation was used to test the asymmetric supercapacitor electrochemical properties. As shown in Figure 7a, CV curves of the Si/MoS_2 composite and AC separately tested in the three-electrode test system indicated that the optimal potential window of Si/MoS_2//AC is 1.5 V, and a good matching for asymmetric supercapacitors. Figure 7b shows CV curves of Si/MoS_2//AC at various scan rates, which show that the pseudocapacitance and double-layer capacitance are common influences on the supercapacitor. The shapes of CV curves were not deformed when the sweep speeds increased, indicating good rate performance. The *C* (specific capacitance (86.9 $F \cdot g^{-1}$)) in the asymmetric capacitor was calculated based on the Figure 7c discharge curves when current density was at 1 $A \cdot g^{-1}$. The Ragone plot is displayed in Figure 7d. The maximum energy density of 27.2 $Wh \cdot kg^{-1}$ is obtained at a power density of 749.1 $Wh \cdot kg^{-1}$, which is more than other reported systems, such as MoS_2-150 mg GF//AEG (16 $Wh \cdot kg^{-1}$/758.2 $W \cdot kg^{-1}$) [6], BCN/MoS_2-31 composite (8.92 $Wh \cdot kg^{-1}$/254.8 $W \cdot kg^{-1}$) [40], PANI-G-MoS_2 (2.65 $Wh \cdot kg^{-1}$/119.2 $W \cdot kg^{-1}$) [41], and MoS_2/RCF electrode (22.5 $Wh \cdot kg^{-1}$/703 $W \cdot kg^{-1}$) [9].

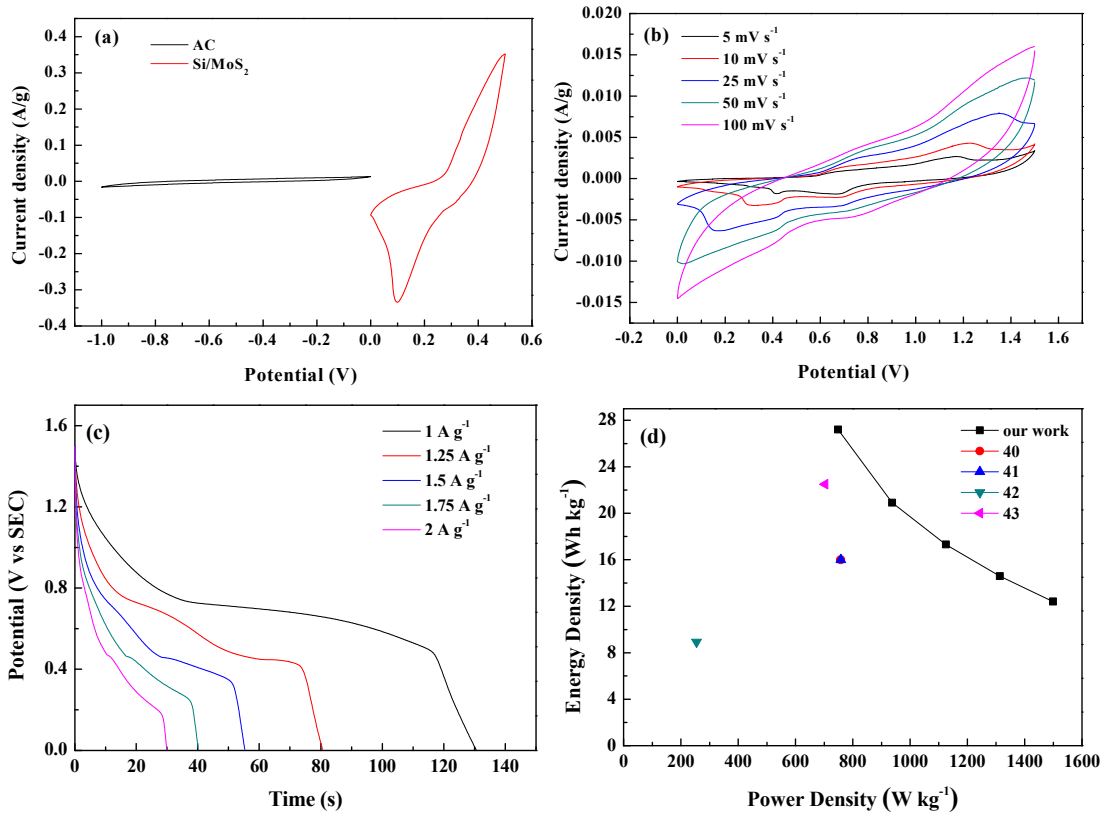

Figure 7. (**a**) CV curve of AC and Si/MoS_2 composite, separately tested in three-electrode system at 100 $mV \cdot s^{-1}$; (**b**) CV curve of asymmetric supercapacitor (Si/MoS_2//AC); (**c**) GCD curve of Si/MoS_2//AC; (**d**) Ragone plots of Si/MoS_2//AC.

4. Conclusions

In this work, microflower-like structure Si/MoS_2 composite was prepared by hydrothermal method. The addition of Si QDs can improve the electrochemical performance of MoS_2. The capacitance of the Si/MoS_2 composite is 574.4 $F \cdot g^{-1}$ at 5 $A \cdot g^{-1}$. When the energy density is 27.2 $Wh \cdot kg^{-1}$, the power density of the Si/MoS_2//AC reaches 749.1 $W \cdot kg^{-1}$. The capacitance retention is 84.5%, even after

1000 cycles. Therefore, the Si/MoS_2 composite microflower will be a great potential electrode material for supercapacitors.

Author Contributions: J.Z. and R.Z. conceived and designed the experiments; R.Z. and K.C. fabricated the sample; Y.Y. and Y.W. characterized the sample; P.Y. oversaw project administration. All authors have read and agreed to the published version of the manuscript.

Funding: The work was funded by National Natural Science Foundation of China (Grant No. 21607013, 5102026), the Natural Science Basic Research Plan in Shaanxi Province of China (2020JM-221), the Fund Project of Shaanxi Key Laboratory of Land Consolidation (2018-JC01), the Fundamental Research Funds for the Central Universities, CHD (300102310203), and Colation and Entrepreneurship Project (201810710127, 201910710466).

Conflicts of Interest: The authors declare no conflict of interest.

References

1. Fu, H.; Zhang, X.D.; Fu, J.Z.; Shen, G.Z.; Ding, Y.L.; Chen, Z.J.; Du, H. Single layers of MoS_2/Graphene nanosheets embedded in activated carbon nanofibers for high-performance supercapacitor. *J. Alloy Compd.* **2020**, *829*, 154557. [CrossRef]
2. Wang, C.; Xu, J.; Yuen, M.; Zhang, J.; Li, Y.; Chen, X.; Zhang, W. Hierarchical composite electrodes of nickel oxide nanoflake 3D graphene for high-performance pseudocapacitors. *Adv. Funct. Mater.* **2014**, *24*, 6372–6380. [CrossRef]
3. Reddy, B.P.; Sekhar, M.C.; Vattikuti, S.V.P.; Suh, Y.; Park, S.H. Solution-based spin-coated tin sulfide thin films for photovoltaic and supercapacitor applications. *Mater. Res. Bull.* **2018**, *103*, 13–15. [CrossRef]
4. Vikraman, D.; Karuppasamy, K.; Hussain, S.; Kathalingam, A.; Sanmugam, A.; Jung, J.; Kim, H.S. One-pot facile methodology to synthesize MoS_2-graphene hybrid nanocomposites for supercapacitors with improved electrochemical capacitance. *Compos. Part B Eng.* **2019**, *161*, 555–563. [CrossRef]
5. Vattikuti, S.V.P.; Reddy, B.P.; Byon, C.; Shim, J. Carbon/CuO nanosphere-anchored g-C_3N_4 nanosheets as ternary electrode material for supercapacitors. *J. Solid State Chem.* **2018**, *262*, 106. [CrossRef]
6. Masikhwa, T.M.; Madito, M.J.; Bello, A.; Dangbegnon, J.K.; Manyala, N. High performance asymmetric supercapacitor based on molybdenum disulphide/graphene foam and activated carbon from expanded graphite. *J. Colloid Interf. Sci.* **2017**, *488*, 155–165. [CrossRef]
7. Yadav, S.K.; Kumar, R.; Sundramoorthy, A.K.; Singh, R.K.; Koo, C.M. Simultaneous reduction and covalent grafting of polythiophene on graphene oxide sheets for excellent capacitance retention. *RSC Adv.* **2016**, *6*, 52945–52949. [CrossRef]
8. Vattikuti, S.V.P.; Devarayapalli, K.C.; Nagajyothi, P.C.; Shim, J. Microwave synthesized dry leaf-like mesoporous $MoSe_2$ nanostructure as an efficient catalyst for enhanced hydrogen evolution and supercapacitor applications. *Microchem. J.* **2020**, *153*, 104446. [CrossRef]
9. Zhao, C.H.; Zhou, Y.N.; Ge, Z.X.; Zhao, C.G.; Qian, X.Z. Facile construction of MoS_2/RCF electrode for high-performance supercapacitor. *Carbon* **2018**, *127*, 699–706. [CrossRef]
10. Xu, C.Y.; Jiang, L.; Li, X.; Li, C.; Shao, C.X.; Zuo, P.; Liang, M.S.; Qu, L.T.; Cui, T.H. Miniaturized high-performance metallic 1T-Phase MoS2 micro-supercapacitors fabricated by temporally shaped femtosecond pulses. *Nano Energy* **2020**, *67*, 104260. [CrossRef]
11. Lia, J.F.; Chen, D.D.; Wu, Q.S. Facile synthesis of CoS porous nanoflake for high performance supercapacitor electrode materials. *J. Energy Storage* **2019**, *23*, 511–514. [CrossRef]
12. Harish, S.; Naveen, A.N.; Abinaya, R.; Archana, J.; Ramesh, R.; Navaneethan, M.; Shimomura, M.; Hayakawa, Y. Enhanced performance on capacity retention of hierarchical NiS hexagonal nanoplate for highly stable asymmetric supercapacitor. *Electrochim. Acta* **2018**, *283*, 1053–1062. [CrossRef]
13. Himasree, P.; Durga, I.K.; Krishna, T.N.V.; Rao, S.S.; Gopi, C.V.V.M.; Revathi, S.; Prabakar, K.; Kim, H.J. One-step hydrothermal synthesis of CuS@MnS on Ni foam for high performance supercapacitor electrode material. *Electrochim. Acta* **2019**, *305*, 467–473. [CrossRef]
14. Kumar, R.; Sahoo, S.; Joanni, E.; Singh, R.K.; Yadav, R.M.; Verma, R.K.; Singh, D.P.; Tan, W.K.; del Pino, A.P.; Moshkalev, S.A.; et al. A review on synthesis of graphene, h-BN and MoS_2 for energy storage applications: Recent progress and perspectives. *Nano Res.* **2019**, *12*, 2655–2694. [CrossRef]
15. Manuraj, M.; Chacko, J.; Unni, K.N.N.; Rakhi, R.B. Heterostructured MoS_2-RuO_2 nanocomposite: A promising electrode material for supercapacitors. *J. Alloy Compd.* **2020**, *836*, 155420. [CrossRef]

16. Lien, C.W.; Vedhanarayanan, B.; Chen, J.H.; Lin, J.Y.; Tsai, H.H.; Shao, L.D.; Lin, T.W. Optimization of acetonitrile/water content in hybrid deep eutectic solvent for graphene/MoS_2 hydrogel-based supercapacitors. *Chem. Eng. J.* **2021**, *405*, 126706. [CrossRef]
17. Vattikuti, S.V.P.; Nagajyothi, P.C.; Reddy, P.A.K.; Kumar, M.K.; Shim, J.; Byon, C. Tiny MoO_3 nanocrystals self-assembled on folded molybdenum disulfide nanosheets via a hydrothermal method for supercapacitor. *Mater. Res. Lett.* **2018**, *6*, 432–439. [CrossRef]
18. Feng, D.; Pan, X.X.; Xia, Q.Y.; Qin, J.H.; Zhang, Y.; Chen, X.M. Metallic MoS_2 nanosphere electrode for aqueous symmetric supercapacitors with high energy and power densities. *J. Mater. Sci.* **2020**, *55*, 713–723. [CrossRef]
19. Voiry, D.; Salehi, M.; Silva, R.; Fujita, T.; Chen, M.W.; Asefa, T.; Shenoy, V.B.; Eda, G.; Chhowalla, M. Conducting MoS_2 Nanosheets as Catalysts for Hydrogen Evolution Reaction. *Nano Lett.* **2013**, *13*, 6222−6227. [CrossRef]
20. Mishra, S.; Maurya, P.K.; Mishra, A.K. 2H–MoS_2 nanoflowers based high energy density solid state supercapacitor. *Mater. Chem. Phys.* **2020**, *255*, 123551. [CrossRef]
21. Wu, D.; Lou, Z.; Wang, Y.; Yao, Z.; Xu, T.; Shi, Z.; Xu, J.; Tian, Y.; Li, X.; Tsang, Y.H. Photovoltaic high-performance broadband photodetector based on MoS_2/Si nanowire array heterojunction. *Sol. Energ. Mat. Sol. C.* **2018**, *182*, 272–280. [CrossRef]
22. Feng, Z.; Yang, P.P.; Wen, G.S.; Li, H.B.; Liu, Y.; Zhao, X.C. One-step synthesis of MoS_2 nanoparticles with different morphologies for electromagnetic wave absorption. *Appl. Surf. Sci.* **2020**, *502*, 144129. [CrossRef]
23. Kumar, R.; Singh, R.K.; Yadav, S.K.; Savu, R.; Moshkalev, S.A. Mechanical pressure induced chemical cutting of boron nitride sheets into boron nitride quantum dots and optical properties. *J. Alloy. Compd.* **2016**, *683*, 38–47. [CrossRef]
24. Singh, R.K.; Kumar, R.; Singh, D.P.; Savu, R.; Moshkalev, S.A. Progress in microwave-assisted synthesis of quantum dots (graphene/carbon/semiconducting) for bioapplications: A review. *Mater. Today Chem.* **2019**, *12*, 282–332. [CrossRef]
25. Erogbogbo, F.; Yong, K.T.; Roy, I.; Hu, R.; Law, W.C.; Zhao, W.W.; Ding, H.; Wu, F.; Kumar, R.; Swihart, M.T.; et al. In vivo targeted cancer imaging, sentinel lymph node mapping and multi-channel imaging with biocompatible silicon nanocrystals. *ACS Nano* **2011**, *5*, 413–423. [CrossRef]
26. Arefi-Oskoui, S.; Khataee, A.; Safarpour, M.; Vatanpour, V. Modification of polyethersulfone ultrafiltration membrane using ultrasonicassisted functionalized MoS_2 for treatment of oil refinery wastewater. *Sep. Purif. Technol.* **2020**, *238*, 116495. [CrossRef]
27. Zhang, X.L.; Ma, L.; Gan, M.Y.; Fu, G.; Jin, M.; Zhai, Y.F. Controllable constructing of hollow MoS_2/PANI core/shell microsphere for energy storage. *Appl. Surf. Sci.* **2018**, *460*, 48–57. [CrossRef]
28. Raza, A.; Ikram, M.; Aqeel, M.; Imran, M.; Ul-Hamid, A.; Riaz, K.N.; Ali, S. Enhanced industrial dye degradation using Co doped in chemically exfoliated MoS_2 nanosheets. *Appl. Nanosci.* **2020**, *10*, 1535–1539. [CrossRef]
29. Zhong, Y.; Sun, X.; Wang, S.; Peng, F.; Bao, F.; Su, Y.; Li, Y.; Lee, S.T.; He, Y. Facile, Large-Quantity Synthesis of Stable, Tunable-Color Silicon Nanoparticles and Their Application for Long-Term Cellular Imaging. *ACS Nano* **2015**, *9*, 5958–5959. [CrossRef]
30. Liu, Z.P.; Hou, J.Z.; Wang, X.F.; Hou, C.J.; Ji, Z.; He, Q.; Huo, D.Q. A novel fluorescence probe for rapid and sensitive detection of tetracyclines residues based on silicon quantum dots. *Spectrochim. Acta A* **2020**, *240*, 118463. [CrossRef]
31. Xu, X.X.; Jiao, S.L.; Liu, Z.Q.; Liu, L. Synergistic lubrication of a porous MoS_2-POSS nanohybrid. *RSC Adv.* **2020**, *10*, 20579. [CrossRef]
32. Yang, Z.M.; Zhang, D.Z.; Chen, H.N. MOF-derived indium oxide hollow microtubes/MoS_2 nanoparticles for NO_2 gas sensing. *Sensor. Actuat. B Chem.* **2019**, *300*, 127037. [CrossRef]
33. Zhao, P.; Tang, Y.; Mao, J.; Chen, Y.; Song, H.; Wang, J.; Song, Y.; Liang, Y.; Zhang, X. One-dimensional MoS_2-decorated TiO_2 nanotube gas sensors for efficient alcohol sensing. *J. Alloy. Compd.* **2016**, *674*, 252–258. [CrossRef]
34. Zhao, S.; Li, Z.; Wang, G.; Liao, J.; Lv, S.; Zhu, Z. Highly enhanced response of MoS2/porous silicon nanowire heterojunctions to NO_2 at room temperature. *RSC Adv.* **2018**, *8*, 11070–11077. [CrossRef]
35. Luo, J.H.; Zhang, K.; Cheng, M.L.; Gu, M.M.; Sun, X.K. MoS_2 spheres decorated on hollow porous ZnO microspheres with strong wideb and microwave absorption. *Chem. Eng. J.* **2020**, *380*, 122625. [CrossRef]
36. Arasi, S.E.; Ranjithkumar, R.; Devendran, P.; Krishnakumar, M.; Arivarasan, A. Electrochemical evaluation of binary $Ni_2V_2O_7$ nanorods as pseudocapacitor electrode material. *Ceram. Int.* **2020**, *46*, 22709–22717. [CrossRef]

37. Guan, B.; Li, Y.; Yin, B.Y.; Liu, K.F.; Wang, D.W.; Zhang, H.H.; Cheng, C.J. Synthesis of hierarchical NiS microflower for high performance asymmetric supercapacitor. *Chem. Eng. J.* **2017**, *308*, 1165–1173. [CrossRef]
38. Huo, H.H.; Zhao, Y.Q.; Xu, C.L. 3D Ni_3S_2 nanosheet arrays supported on Ni foam for high-performance supercapacitor and nonenzymatic glucose detection. *J. Mater. Chem. A* **2014**, *2*, 15111–15117. [CrossRef]
39. Peng, W.J.; Wang, W.; Han, G.H.; Huang, Y.K.; Zhang, Y.S. Fabrication of 3D flower-like MoS_2/graphene composite as highperformance electrode for capacitive deionization. *Desalination* **2020**, *473*, 114191. [CrossRef]
40. Thakur, A.K.; Majumder, M.; Choudhary, R.B.; Singh, S.B. MoS_2 flakes integrated with boron and nitrogen-doped carbon: Striking gravimetric and volumetric capacitive performance for supercapacitor applications. *J. Power Sources* **2018**, *402*, 163–173. [CrossRef]
41. Palsaniya, S.; Nemade, H.B.; Dasmahapatra, A.K. Synthesis of polyaniline/graphene/MoS_2 nanocomposite for high performance supercapacitor electrode. *Polymer* **2018**, *150*, 150–158. [CrossRef]